Delft University of Technology

Membrane area gain and loss during cytokinesis

Frey, Felix; Idema, Timon

Citation (APA)

Important note
To cite this publication, please use the final published version (if applicable).
Please check the document version above.

Membrane area gain and loss during cytokinesis

Felix Frey and Timon Idema[*]

Department of Bionanoscience, Kavli Institute of Nanoscience, Delft University of Technology, Van der Maasweg 9,
2629 HZ Delft, The Netherlands

In cytokinesis of animal cells, the cell is symmetrically divided into two. Since the cell's volume is conserved, the projected area has to increase to allow for the change of shape. Here we aim to predict how membrane gain and loss adapt during cytokinesis. We work with a kinetic model in which membrane turnover depends on membrane tension and cell shape. We apply this model to a series of calculated vesicle shapes as a proxy for the shape of dividing cells. We find that the ratio of kinetic turnover parameters changes nonmonotonically with cell shape, determined by the dependence of exocytosis and endocytosis on membrane curvature. Our results imply that controlling membrane turnover will be crucial for the successful division of artificial cells.

I. INTRODUCTION

One of the hallmarks of living systems is their ability to replicate and spread, achieved through division at the cellular level [1–3]. In cytokinesis, the last step of cell division, one cell is split into two daughter cells of equal size [cf. Fig. 1(a)] [4,5]. The change of shape is best characterized by the cellular volume and the projected area, which is defined by the minimal area needed to enclose a volume at given shape [6]. Experimentally, it has been found that cells divide at constant volume [7–9], implying that the projected area increases.

The cellular volume is controlled by mechanical forces, material fluxes, and water fluxes between the inside of the cell and its environment [10]. The projected area of the cell is determined by the volume and shape and regulated by the total membrane area. In contrast to the projected area, the total membrane area of the cell includes area that is stored in fluctuations and membrane reservoirs. Since the size of membrane reservoirs can be large, the total membrane area can be more than twice the projected area [11,12]. In general, membrane trafficking by exocytosis and endocytosis regulates the total membrane area [6]. Therefore, half of the membrane area can be recycled in about 1 h [13]. Similar to the projected area, the total membrane area increases during cytokinesis [14], maintained through a changed ratio between exocytosis and endocytosis [14–16]. For example, it has been estimated that over 600 vesicles have to fuse with the cell membrane during the division of fission yeast [17]. The exocytotic and endocytotic rates are expected to be influenced by membrane tension [18]. Moreover, membrane shape and curvature influence membrane trafficking [19,20]. However, how membrane trafficking adapts to the shape changes during cytokinesis is largely unknown [21].

In general, the shape of animal cells is controlled through the actomyosin cortex [6,22]. During cytokines, the change of cell shape is driven through the constriction of the actomyosin

ring [23]. To ensure robust membrane constriction, the process is highly regulated and thus complex [24]. Potentially, a mechanism for cell division could have been relatively simple (at least in its original form) [25], as it has to be among the first functions that protocells have attained during evolution. This notion is supported by the fact that many of the working principles underlying cytokinesis are conserved across different organisms [17,26].

Similar to protocells, minimal functionality will be the starting point for building artificial cells [27,28]. When devising artificial cells, usually lipid vesicles are equipped with the basic functionality of a living cell. Besides the ability to divide, such vesicles also need to have the ability to grow and take up particles, with the consequence that the total membrane area can increase or decrease. The resulting biomimetic systems—here called functionalized vesicles (FUVs)—can be considered as highly simplified, artificial cells. Although the division mechanisms and internal mechanics of FUVs are simplified compared to biological cells [29–33], similar to cells and dictated by geometry, FUVs must increase their projected area during division at constant volume. Therefore, for both cells and FUVs, the question remains how membrane turnover and division can be compatible with each other [34].

In this paper, we theoretically investigate the interplay between shape changes and membrane trafficking during cytokinesis, following the assumption that the interior of the cell can be inferred from modeling membrane deformations [35]. Our analysis consists of two steps. First, we calculate the shapes of dividing FUVs as a proxy for cell shapes. Second, we use these shapes to extrapolate how membrane trafficking changes during cytokinesis.

We base our assumption to treat the shapes of dividing FUVs as a proxy for cell shapes on two observations: First, the timescales of mechanical membrane relaxation [36] [cf. Fig. 1(b)] and membrane turnover [17] [cf. Fig. 1(c)], are much faster than the timescale of membrane-shape changes during cell division [17] [cf. Fig. 1(d)]. Based on these observations, we assume that the timescales of the processes

—————
[*]t.idema@tudelft.nl

(a) Cytokinesis

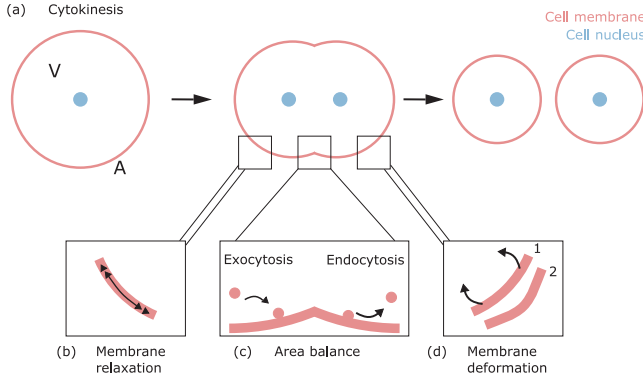(b) Membrane relaxation   (c) Area balance   (d) Membrane deformation

FIG. 1. Membrane shape and membrane dynamics during cytokinesis. (a) During cytokinesis, a rounded-up cell splits into two daughter cells of equal size. While the projected area A of the cell increases, the cellular volume V is kept constant. Several processes influence the shape and the total membrane area. (b) Since membrane area is laterally redistributed on a short timescale, the membrane relaxes rapidly toward its equilibrium shape. (c) On an intermediate timescale, the total membrane area is determined by membrane turnover. Total membrane area gain is driven through exocytosis, whereas total membrane area loss is driven through endocytosis. Both exocytosis and endocytosis act along the projected area. (d) On a large timescale, the membrane shape changes.

acting on the membrane are well separated. Therefore, we assume that the shapes of dividing cells can be considered as quasiequilibrium shapes. Second, although the underlying mechanics are different, the shapes of dividing cells and vesicles are relatively similar [30,37]. We conclude that it is possible to treat the shapes of dividing FUVs as a proxy for dividing cell shapes.

We calculate the shapes of dividing FUVs with rotational symmetry by minimizing their shape energy. The change in shape during division is driven by a reduction of the reduced volume (i.e., the ratio of FUV volume to projected area) and an increase of the preferred curvature (i.e., the membrane's tendency to curve). In addition, the volume of the FUV is kept constant during division.

Next, we develop a phenomenological model for the total membrane area that balances area gain and loss, using the membrane shape as input. We assume that the increase in total membrane area during cytokinesis is proportional to the increase in projected membrane area, as measured for cells in the absence of membrane reservoirs [14]. Moreover, in the model, we assume that exocytosis is globally controlled by the amount and tension of intracellular membrane and that endocytosis is globally controlled by the tension of the cell membrane. In addition, we assume that exocytosis and endocytosis are influenced locally by the shape of the membrane, mediated by the mean membrane curvature. By using the calculated FUV shapes in the membrane area balance equation at steady state, we then predict how the ratio between membrane gain and loss has to evolve during the division process. We find that this ratio changes nonmonotonically during cytokinesis, suggesting a complex interplay between membrane shape change and membrane trafficking.

II. SHAPES OF DIVIDING VESICLES AS A PROXY FOR DIVIDING CELL SHAPES

The change of shape during cytokinesis can be characterized by the volume V and the projected area A of the cell. During division, either the volume or the projected area could be conserved. While volume conservation implies that the projected area has to increase, projected area conservation implies that the volume has to decrease. Volume and projected area can be combined into the reduced volume $\nu = 3V/(4\pi (A/4\pi)^{3/2})$, with $\nu = 1$ for spheres and $\nu < 1$ for all other shapes. From a geometrical perspective, we can generate identical values for ν, independent of whether we change the projected area A or volume V. Obviously, the qualitative symmetry when changing A or V occurs because in the expression of the reduced volume the cell size is scaled out. For a cell, however, size matters because the cell uses many resources to produce the material contained within its volume. Consequently, a volume loss is disadvantageous. Moreover, to reach the same value of ν, the relative increase in projected area is smaller than the relative decrease in volume. Hence, it is theoretically predicted and experimentally confirmed that cytokinesis occurs at constant volume [7–9]. Therefore, shape changes during cytokinesis have to be accompanied by an increase of the projected area A. If we assume a symmetric division of an initially spherical cell into two spherically shaped daughter cells at constant volume, the fission limit of the reduced volume is $\nu = 1/\sqrt{2}$. For larger values of ν, only asymmetric division is possible. We conclude that symmetric division requires large projected area gain that has to be driven from the interior of the cell.

Symmetric division also requires a mechanism by which the membrane shape can change in a manner compatible with the gain of the projected area. In the cell, the membrane is deformed by the constriction of the actomyosin contractile ring. For simplicity, we use the shapes of dividing FUVs as a proxy for dividing cell shapes. In FUVs, the division process can be driven by increasing the preferred or spontaneous curvature and decreasing the reduced volume, as demonstrated experimentally [30,32]. In FUVs, the shape of the membrane is the one that minimizes the total energy [38–40]. To describe the membrane shape energy, different models can be used, for example, the spontaneous curvature model or the area-difference elasticity model [41–45]. Importantly, the area-difference elasticity model can be connected to the spontaneous curvature model, which allows us to switch between the two descriptions [40,46]. In the following, we use the spontaneous curvature model. In this case, the membrane shape energy reads

$$\mathcal{H} = 2\kappa \int (H - H_0)^2 \, dA + \Sigma A - \Delta P V, \qquad (1)$$

where the first term is the bending energy of the membrane, with κ the bending rigidity, $H = (C_1 + C_2)/2$ the mean membrane curvature, where C_1 and C_2 are the principal curvatures, and H_0 the preferred or spontaneous curvature of the membrane. The second and third terms include constraints on the projected area A and the enclosed volume V by means of the two Lagrange multipliers, which are the vesicle membrane tension Σ and the pressure difference $\Delta P = P_{\text{in}} - P_{\text{out}}$

between the inside and outside of the vesicle. In general, Eq. (1) could contain an additional integral running over the Gaussian curvature [47]. However, by the Gauss-Bonnet theorem, this contribution only adds up to a constant if it is calculated for a closed vesicle that does not change its topology. Thus, the term has no effect on the vesicle shape [47]. Since we are only interested in the shapes of vesicles without topological changes, we can neglect this contribution in the following.

Following Refs. [39,40], we can calculate the shape equations that determine the vesicle shapes from Eq. (1). To control the shape of membrane vesicles, we use the common parameters of reduced volume v and reduced preferred curvature $\bar{H}_0 = H_0 R_{ve}$, with the vesicle radius $R_{ve} = \sqrt{A/(4\pi)}$ [39–41]. Alternatively, the vesicle shapes could be described by the reduced area $A/A_s = A/(4\pi(3V/(4\pi))^{2/3})$, which normalizes the projected area A of the vesicle shape by the area $A_s = 4\pi(3V/(4\pi))^{2/3}$ of a sphere with the same volume, and the spherical reduced preferred curvature $\bar{H}_0^s = H_0 R_s$, which normalizes the preferred curvature H_0 by the radius of the sphere with the same volume $R_s = (3V/(4\pi))^{1/3}$. Since we assume that internal membrane redistribution is faster than membrane trafficking, we expect that the vesicle relaxes toward an axisymmetric configuration, and thus we deal with the shape equations of axisymmetric vesicles. To solve the shape equations numerically, we closely follow the procedure outlined in detail in Ref. [40] and summarized in Appendix A. Importantly, after setting v and $\bar{H}_0$, we find the minimal energy membrane shapes by adapting the Lagrange multipliers Σ and ΔP such that the shape equations are fulfilled.

To investigate how membrane trafficking has to adapt during cytokinesis, we calculate FUV shapes that resemble a dividing cell. Although v and $\bar{H}_0$ are both functions of the projected area A, they can change independently. To generate dividing vesicle shapes, changing the reduced volume v alone would not be sufficient, as we would only obtain prolate- or oblate-shaped vesicles [39]. Therefore, to obtain the shape of dividing vesicles, we also increase the preferred curvature $\bar{H}_0$, according to the state diagram for lipid vesicles [39,40]. In general, there are many possible ways of combining the changes in v and $\bar{H}_0$. Here, we calculate two sequences of vesicle shapes to investigate the effect of variations in membrane shape on membrane trafficking during cytokinesis. We note that the exact choice of v and $\bar{H}_0$ is of no particular importance, except for the fact that these FUV shapes are taken as ξ proxy for a dividing cell.

In Fig. 2(a), we calculate FUV shapes by first decreasing v from 1 to 0.7 at $\bar{H}_0 = 0$. Subsequently, we increase $\bar{H}_0$ from 0 to 1.41 at constant $v = 0.7$. Since v and $\bar{H}_0$ are changed one after the other, we refer to this as the sequential change sequence. In contrast, in Fig. 2(b), we calculate FUV shapes where we decrease v from 1 to 0.7 while simultaneously increasing $\bar{H}_0$ from 0 to 1. Subsequently, $\bar{H}_0$ is further increased from 1 to 1.41 at constant $v = 0.7$. Since v and $\bar{H}_0$ are changed in parallel, we refer to this as the parallel change sequence. At $v = 1/\sqrt{2} \approx 0.71$ and $\bar{H}_0 = \sqrt{2} \approx 1.41$, we expect to find the fission limit, which is the minimal reduced volume and reduced preferred curvature that is needed to form a two-sphere configuration with a closed membrane neck [40]. The two shape sequences in Fig. 2 thus represent membrane shapes
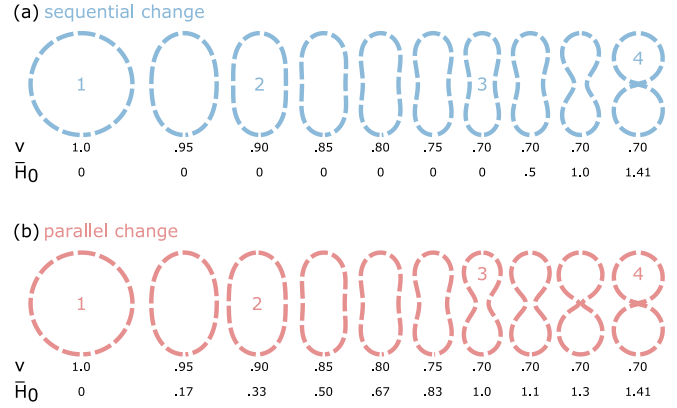

FIG. 2. Calculated FUV shapes, mimicking the shapes of dividing cells. (a) Sequential change sequence, where first the reduced volume v is decreased from 1 to 0.7 and then the reduced preferred curvature $\bar{H}_0$ is increased from 0 to 1.41. (b) Parallel change sequence, where the reduced volume v and the preferred curvature $\bar{H}_0$ are changed simultaneously. While v is decreased from 1 to 0.7, $\bar{H}_0$ is increased from 0 to 1. Subsequently, and similar to (a), $\bar{H}_0$ is increased from 1 to 1.41, while $v = 0.7$ is kept constant.

of splitting FUVs, calculated from membrane mechanics. In Tables I and II in Appendix B, we summarize the reduced volume v, the reduced preferred curvature $\bar{H}_0$, the spherical vesicle radius R, the volume V, the projected area A, the reduced area A/A_s, and the spherical reduced preferred curvature $\bar{H}_0^s$ for the sequential and parallel change sequence in Figs. 2(a) and 2(b). We note that for all shapes presented in Fig. 2, the mean curvature is positive on the whole shape.

III. MODELING MEMBRANE TRAFFICKING AND AREA BALANCE

During cytokinesis at constant volume, the projected area increases, which is coupled to the total membrane area. In the following, we formulate a kinetic model for the dynamics of the total membrane area $\mathbb{A}$. Importantly, the model does not describe how the change of cell shape occurs. Instead, the model takes the shape as input to determine membrane trafficking. In the model, we assume that the volume is controlled independently of the total membrane area and kept constant. Moreover, we assume that the membrane turnover and redistribution of the membrane area density $\xi(\boldsymbol{r}, t)$ (the local membrane area per projected unit area) is regulated by exocytosis and endocytosis that bring material to and take material away from the cell membrane [48].

In the cell, exocytosis and endocytosis are complex processes that within the scope of our model are greatly simplified. Membrane area gain through exocytosis is mediated by the fusion of lipid vesicles with the cell membrane. We assume that exocytosis is globally controlled by the amount and tension of internal membrane area in the way that area addition gets easier with a bigger internal membrane area reservoir a_i and anticorrelates with the internal tension Γ_i [49] [cf. Fig. 3(a)].

Moreover, membrane fusion requires close contact between the two fusing bilayer membranes, before hemifusion,
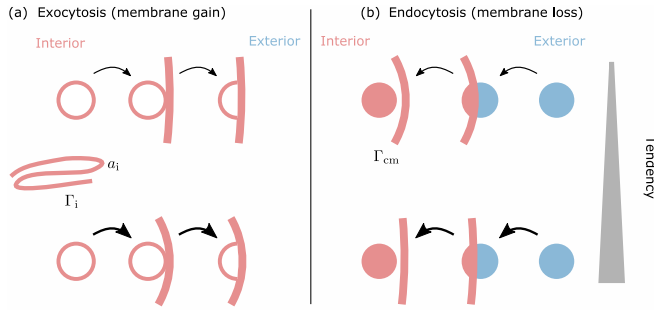
FIG. 3. Membrane gain through exocytosis and membrane loss through endocytosis. (a) In our model, membrane gain depends on the amount of internal membrane area a_i and is inversely proportional to the internal membrane tension Γ_i. Moreover, the tendency for exocytosis is low for a nearly flat membrane since the contact area between the vesicle (red sphere) and the membrane (red line) is small (top). The tendency for exocytosis increases when the membrane is more curved since the contact area between the vesicle and the membrane increases (bottom). (b) In our model, membrane loss is inversely proportional to the tension of the cell membrane Γ_{cm}. Moreover, the tendency for endocytosis is low for a curved membrane since the contact area between the particle (blue sphere) and the membrane (red line) is small (top). The tendency for endocytosis increases for a nearly flat membrane since the contact area between the particle and the membrane increases (bottom).

followed by full fusion, can occur. The rate-limiting step for membrane fusion is the docking between the two membranes [50]. The efficiency of generating the contact area increases with the surface density of linker proteins [51]. Given a homogenous distribution of linkers on the membrane surface, we assume that the number of linkers that can make actual contact with the vesicle is proportional to the contact area between the vesicle and the cell membrane. This contact area increases with membrane curvature [cf. Fig. 3(a)]. Therefore, we assume that exocytosis is proportional to the (local) mean curvature $H = (C_1 + C_2)/2$ along the FUV's projected area, where C_1 and C_2 are the principal curvatures. The assumption is in agreement with the work of Nomura *et al.*, who found that large unilamellar vesicles (with large curvature) can fuse with each other, while large and giant unilamellar vesicles (with smaller curvature) cannot fuse [52].

Wrapping a particle into the membrane during endocytosis has the side effect that the total membrane area decreases [53]. Thus, endocytosis leads to membrane area loss. In general, the rate of endocytosis anti-correlates with membrane tension [54]. Therefore, we assume that endocytosis or particle uptake is globally reduced with increasing cell membrane tension Γ_{cm} [49] [cf. Fig. 3(b)].

In the cell, one of the main uptake routes is clathrin-mediated endocytosis [55]. In clathrin-mediated endocytosis, a clathrin coat is assembled at the cell membrane, which drives vesicle formation and particle uptake. The process is facilitated when the membrane is curved in the direction of the nascent membrane bud [56]. In our model, we consider a spherical cell shape initially, which implies that the membrane is curved outward. When increasing the curvature with respect to the initial spherical state, the membrane will curve away

from the particle that is taken up. In contrast, when decreasing the curvature of the cell, the membrane will curve toward the particle that is taken up. Since the contact area between the membrane and the particle that is supposed to be taken up decreases with curvature [cf. Fig. 3(b)], we assume that material uptake decreases with local membrane curvature. Therefore, and to include the mean curvature into the area gain and loss term symmetrically, we assume that endocytosis is antiproportional to the (local) mean curvature H along the FUV's projected area. Importantly, the assumptions on the curvature dependence of endocytosis are in agreement with theoretical modeling for spherical vesicles, which suggests that the parameter space for complete uptake increases with increasing vesicle size [57].

Combined, the balance or continuity equation for the change in membrane area density reads

$$\dot{\xi} + \nabla \cdot (\xi \boldsymbol{v}) = J\left(\frac{a_i}{\Gamma_i}H - \frac{1}{\Gamma_{cm}}\frac{1}{H}\right). \qquad (2)$$

The first term on the left-hand side of Eq. (2) describes how the membrane area density changes in time. The second term describes how the membrane area density is spatially redistributed, representing how lipids rearrange after membrane gain or loss. In this context $\boldsymbol{v}$, is the membrane transport velocity field. The first term on the right-hand side describes the area gain and the second term the area loss. In order to match the dimensions of the equation, the right-hand side has to be multiplied with a material transport coefficient J, which carries the units of energy per volume and time.

There are three processes involved in membrane trafficking during cytokinesis, with clearly separated timescales. On the fastest timescale (<1 s), the membrane mechanically relaxes because lipids within the membrane rearrange to reach a homogenous distribution [36] [cf. Fig. 1(b)]. On the intermediate timescale (~30 s), membrane turnover is maintained due to total membrane area gain and loss [17] [cf. Fig. 1(c)]. On the slowest timescale (~30 min), the membrane shape changes, since the actomyosin ring constricts the cell membrane [17,23] [cf. Fig. 1(d)]. In principle, Γ_i and Γ_{cm} can change on the same timescale as the membrane deforms. Considering that mechanical membrane relaxation is much faster than membrane trafficking and the mechanisms that drive membrane deformations, we can rewrite Eq. (2). Effectively, the separation of timescales implies that the membrane area density will not be advected anymore, hence $\boldsymbol{v} = 0$. Therefore, the second term on the left-hand side of Eq. (2) equates to zero. We can integrate the equation along the projected area of the membrane and find the time evolution for the total membrane area,

$$\dot{\mathbb{A}} = k_{on} \int H \, dA - k_{off} \int \frac{1}{H} \, dA, \qquad (3)$$

with $k_{on} = Ja_i/\Gamma_i$ and $k_{off} = J/\Gamma_{cm}$. We note that the kinetic turnover parameters k_{on} and k_{off} carry different units. While k_{on} scales as length per time, k_{off} scales as one over length and time. The reason for this is that the membrane shape affects membrane gain and loss differently in Eqs. (2) and (3). The prediction of how the ratio of kinetic turnover parameters

changes during cytokinesis will be the main result of this paper.

Importantly, the left-hand side of the Eq. (3) describes the total membrane area, including membrane area stored in fluctuations and membrane reservoirs such as caveolae or membrane wrinkles. The integrals on the right-hand side of the equation describe the change of the total membrane area related to exocytosis and endocytosis. Both processes are determined by the local shape. Therefore, the integrals on the right-hand side of the equation are taken along the projected area of the cell, along which the mean curvature is determined. The separation of timescales for membrane relaxation, membrane turnover, and membrane deformation implies that the local membrane area density is homogenous. Therefore, the local membrane area density does not influence exocytosis and endocytosis locally.

In the limiting case where the area gain and loss terms are independent of the mean curvature H, and assuming a homogeneous area density β so the total membrane area and the projected area are proportional to each other, we recover the simple growth law for the projected area $\dot{A} = (k_{\text{on}} - k_{\text{off}})A/\beta$, similar to a recent model for prebiotic vesicles [34]. However, in this case, k_{on} and k_{off} carry the physical unit of rates, namely, s^{-1}, and $k_{\text{on}} - k_{\text{off}}$ becomes an effective growth rate. Before we turn toward the main results of our paper, we briefly discuss the stability behavior of Eq. (3).

First, we consider the stability behavior with respect to size deformations (cf. Appendix C). For simplicity, we fix the initial spherical shape and neglect the difference between projected area and total membrane area. However, for the sake of the argument, we allow for changes in the size (and volume). In this case, we find that the area balance equation leads to a stable size with radius $R_{\text{s}} = \sqrt{k_{\text{on}}/k_{\text{off}}}$ and projected area $A_{\text{s}} = 4\pi k_{\text{on}}/k_{\text{off}}$ (cf. Appendix C). The result suggests an interpretation of $k_{\text{on}}/k_{\text{off}}$: For any shape, there is a value of this ratio, corresponding to an area, for which the area balance equation is at steady state. We can also show that this particular stability behavior is a more general property of the area balance equation. It also holds true for other choices of how the total membrane area gain and loss depend on membrane curvature (cf. Appendixes C and E). However, a modified area balance equation with curvature independent area gain and loss terms would not lead to a stable cell size (cf. Appendix C).

Second, we consider the stability behavior with respect to shape deformations (cf. Appendix D). For simplicity, we again neglect the difference between projected area and total membrane area. Moreover, we fix the volume and allow for the shape to change. For this purpose, we expand Eq. (3) in spherical harmonics around the initial spherical state with the usual parameters l and m. We choose to analyze the prolate mode ($l = 2$, $m = 0$). For these particular shapes, we find that the membrane deformations are stable, meaning that they will not trigger any additional total membrane area gain.

To conclude, Eq. (3) defines an area balance equation that is both phenomenologically and geometrically reasonable, connecting finite total membrane areas with stable membrane shapes.

IV. MEMBRANE TURNOVER ADAPTS DURING CYTOKINESIS

During cell division, the projected area of the cell increases at constant volume and with continuous membrane trafficking. In principle, the increase in projected area can be regulated by the addition of lipids through membrane trafficking, through membrane reservoirs or through a combination of both sources. While in the first and third case the total membrane area increases, in the second case the total membrane area stays constant. In the model, we assume that the total membrane area increases due to membrane trafficking at a homogeneous membrane area density. The assumption is confirmed by experimental measurements that show that during cytokinesis the increase in total membrane area is approximately similar to the increase in projected area, in the absence of membrane reservoirs [14]. Moreover, the timescales for membrane relaxation, membrane turnover, and membrane deformation separate during cytokinesis. Thus, we can consider the cell as if going through a sequence of quasiequilibrium shapes during cytokinesis. Then, we can treat Eq. (3) at the steady state for each shape, where the membrane gain and loss have to balance exactly,

$$0 = k_{\text{on}} \int H \, dA - k_{\text{off}} \int \frac{1}{H} \, dA, \tag{4}$$

and hence

$$\frac{k_{\text{off}}}{k_{\text{on}}} = \frac{\int H \, dA}{\int \frac{1}{H} \, dA}. \tag{5}$$

To determine how the ratio of membrane gain and loss has to adapt during cytokinesis, we introduce the dimensionless gain/loss factor γ. The gain/loss factor γ determines the ratio of k_{on} and k_{off} with respect to the kinetic turnover parameters of the initial spherical state k_{on}^{s} and $k_{\text{off}}^{\text{s}}$, for which the area balance equation is at steady state. We get

$$\gamma = \frac{k_{\text{on}}^{\text{s}}}{k_{\text{off}}^{\text{s}}} \frac{k_{\text{off}}}{k_{\text{on}}} = v^{\frac{2}{3}} R_{\text{ve}}^2 \frac{\int H \, dA}{\int \frac{1}{H} \, dA}, \tag{6}$$

where we used Eq. (5), $k_{\text{on}}^{\text{s}}/k_{\text{off}}^{\text{s}} = R_{\text{s}}^2$ and the identity $R_{\text{s}}^2 = v^{2/3} R_{\text{ve}}^2$. Importantly, γ can also be expressed as the ratio between Γ_{cm} and Γ_{i} (cf. Appendix D). From Eq. (6), we see that γ is influenced both by the projected area A and the mean curvature H, which together define the membrane shape. Hence, γ can only be computed after computing the shape from Eq. (1).

To determine how γ changes during cytokinesis, we use the quasiequilibrium FUV shapes as a proxy for dividing cell shapes. We thus apply Eq. (6) on the FUV shapes of Fig. 2. Figure 4 shows γ as a function of the reduced area $A/A_{\text{s}} = (1/v)^{2/3}$ [Fig. 4(a)] and as a function of the reduced preferred curvature $\bar{H}_0$ [Fig. 4(b)]. Along the curves, several data points are marked corresponding to the numbered shapes in Fig. 2. The initial sphere has both $v = 1$ and $\gamma = 1$. As we deform the sphere, we find that γ first decreases before it increases again, both for the sequential change sequence (dashed blue line) and for the parallel change sequence (dashed red line). At $A/A_{\text{s}} = (1/0.71)^{2/3} \approx 1.26$, the fission limit occurs (gray solid line), which is the relative projected area increase that is needed to split one sphere into two spheres at equal volume.
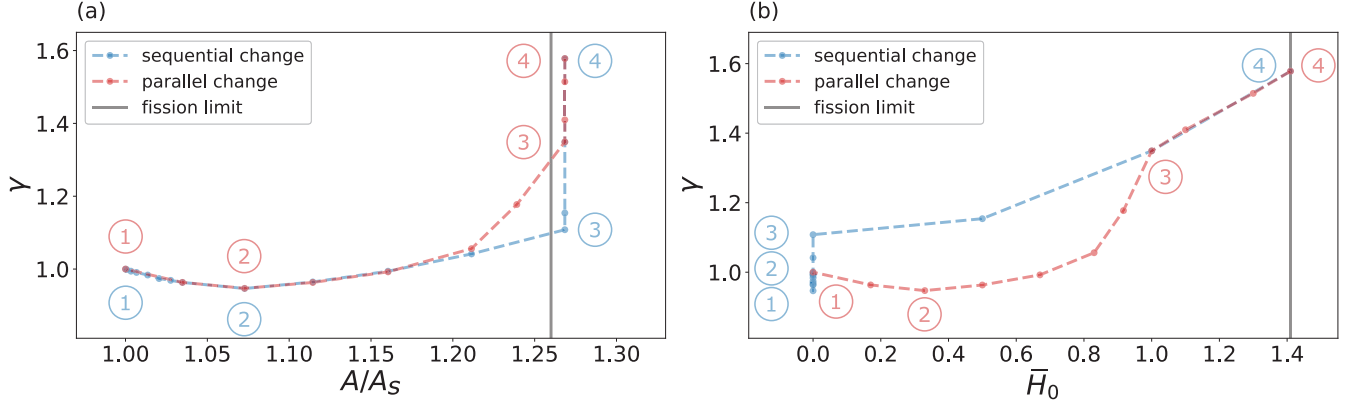
FIG. 4. Membrane trafficking predicted for the shapes as displayed in Fig. 2. (a) The gain/loss factor γ as a function of the reduced area A/A_s. For the sequential change sequence (dashed blue line), γ first decreases with increasing A/A_s before it increases. Then, γ increases at a constant reduced area of around $A/A_s = 1.27$ toward the end of the sequence since here only the reduced preferred curvature increases. For the parallel change sequence (dashed red line), we find qualitatively similar behavior. At $A/A_s \approx 1.26$, the fission limit is marked as a gray line. (b) The gain/loss factor γ as a function of the reduced preferred curvature $\bar{H}_0$. For the sequential change sequence (blue), γ first decreases and then increases at constant $\bar{H}_0$ before it increases monotonically with increasing $\bar{H}_0$. For the parallel change sequence (red), γ first decreases before it increases again with increasing $\bar{H}_0$. At $\bar{H}_0 \approx 1.41$, the fission limit is marked as a gray line.

At the value $A/A_s = (1/0.7)^{2/3} \approx 1.27$, the data points lie on a vertical line because the change of shape is due to the increase in $\bar{H}_0$. Close to the fission limit the blue and red curves differ, since different values of $\bar{H}_0$ result in different FUV shapes. Figure 4(b) shows γ as a function of $\bar{H}_0$. Of course, we again find that γ changes non-monotonically, although it is less obvious for the sequential change sequence since the change occurs at $\bar{H}_0 = 0$. At $\bar{H}_0 = \sqrt{2} \approx 1.41$, the fission limit occurs (gray solid line), which is the minimal reduced preferred curvature that is needed to form a two-sphere configuration with a closed membrane neck.

In Fig. 5, we show γ as a function of ν for the sequential change sequence (dashed blue line) and the parallel change sequence (dashed red line). Along the curves, we also plot the shapes of Fig. 2. Starting from the initial spherical shape at $\nu = 1$, we observe that γ first decreases until it reaches its minimal value for $\nu \approx 0.9$. Only then, γ increases until division is complete. Both the sequential change sequence and the parallel change sequence are quite similar at the beginning because the shapes of Fig. 2 are comparable. Only when $\nu \approx 0.75$, the shapes become considerably different and the curves diverge.

To get analytical insight into the nonmonotonic behavior of γ as a function of ν, it is rewarding to consider a spherocylinder. We choose the spherocylinder to have the same volume as the shapes considered in Fig. 2. For a spherocylinder, the volume and projected area can be expressed by means of the radius R_{sphero} and the aspect ratio $AR = L/R_{\text{sphero}}$. In the expression for AR, L is the length of the cylindrical part. $L = 0$ corresponds to the limiting case of a sphere and implies $AR = 0$. The volume and projected area of the spherocylinder read $V_{\text{sphero}} = \pi R_{\text{sphero}}^3 (4/3 + AR)$ and $A_{\text{sphero}} = 2\pi R_{\text{sphero}}^2 (2 + AR)$, so the reduced volume is given by

$$\nu(AR) = \frac{1 + \frac{3}{4}AR}{\left(1 + \frac{AR}{2}\right)^{\frac{3}{2}}}. \tag{7}$$

By using the mean curvature of the spherical and cylindrical part, $1/R_{\text{sphero}}$ and $1/(2R_{\text{sphero}})$, respectively, and the expression for the projected area on Eq. (6), we find

$$\gamma(AR) = \frac{(1 + \frac{3}{4}AR)^{\frac{2}{3}}}{1 + \frac{AR}{2}} \frac{(2 + AR)(4 + AR)}{8(1 + AR)}. \tag{8}$$

By numerically inverting Eq. (7) and using the result in Eq. (8), we get $\gamma(\nu)$ for the spherocylinder, which is plotted in
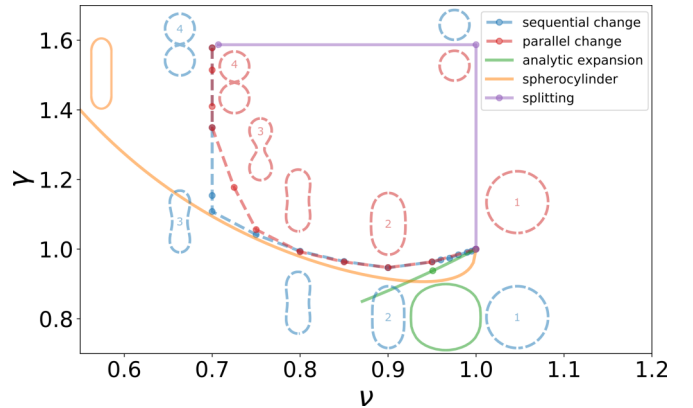

FIG. 5. Predicted membrane turnover for various shapes. We plot the ratio of the gain/loss factor γ as a function of the reduced volume ν for various cases. The sequential change and parallel change sequences from Fig. 2 are shown in dashed blue and red, respectively. For both sequences, γ first decreases with decreasing ν before it increases again with decreasing or constant ν. The corresponding membrane shapes are plotted along the curves in the corresponding colors. As a limiting case, γ is also shown for a spherocylinder of increasing length (solid orange). The solution from the expansion in spherical harmonics around the sphere (solid green) agrees with the numerical solutions when $\nu \approx 1$. In purple, the analytic values are shown for two connected spheres, a small sphere and a large sphere to show how γ is predicted to change during the whole sequence of shapes during FUV division.

solid orange in Fig 5. Importantly, we see that the spherocylinder shows the same non-monotonic behavior as the sequential and the parallel change sequence.

To understand the nonmonotonic change of γ for the different shapes, it is informative to revisit Eq. (4). Increasing the mean curvature increases the term associated with area gain. In contrast, increasing the mean curvature decreases the term associated with area loss. For shapes deviating from the spherical shape, the mean curvature will increase in general. Therefore, to balance area gain and loss, Eq. (4) implies that γ has to increase to compensate. However, for some shapes the mean curvature is reduced locally and therefore the area gain term decreases and the area loss term increases. In this case, γ has to decrease to balance area gain and loss.

We can also compare our results with our analytical expansion of Eq. (3) in spherical harmonics in Appendix D. In the expansion, for simplicity, we consider only shapes of the prolate mode ($l = 2$, $m = 0$). For this particular shape, we can relate ν to γ. The result (green solid line) and the corresponding shape for $\nu = 0.95$ (green) are both shown in Fig. 5. As expected, we only see agreement between the numerically calculated shapes and our analytical approximation close to the sphere ($\nu \approx 1$). When deviating from the sphere, the green line monotonically decreases, which indicates that our expansion of Eq. (3) does not hold true anymore.

To predict how membrane trafficking adapts during cell division, we calculate three more values of $\gamma(\nu)$. First, for two spheres with closed membrane neck of initial spherical volume V_s; second, for a single sphere of half the initial volume V_s; and third, for a single sphere of volume V_s (solid purple line). The blue or red line together with the purple line then form a closed trajectory that can represent a full cell cycle. From this closed curve, we can read off our main result: the non-monotonic change of the gain/loss factor γ necessary for cytokinesis.

To test the robustness of our results and to study the underlying physical mechanisms, we investigate two variants of Eq. (3). First, we neglect the curvature dependence of the membrane loss term so that we get $\dot{\mathbb{A}} = k_{on} \int H \, dA - k_{off} A$ (simple loss model). In this case, k_{on} carries the units of a velocity and k_{off} of a rate. Second, we neglect the curvature dependence of the membrane gain term, so we get $\dot{\mathbb{A}} = k_{on} A - k_{off} \int 1/H \, dA$ (simple gain model). Now k_{on} carries the unit of a rate and k_{off} carries the units of one over length and time. In both cases, the area balance equation has a stable fixed point for spherical shapes with radius $R_s = k_{on}^s/k_{off}^s$ (cf. Appendix E). Similar to before, we evaluate the simple loss equation and the simple gain equation at steady state. We calculate γ for both the sequential change sequence and the parallel change sequence from Fig. 2 and for the spherocylinder (cf. Appendix E).

In Fig. 6(a), we plot γ as function of ν for the sequential change sequence (dashed blue line), the parallel change sequence (dashed red line), and the spherocylinder (solid orange line) for the simple loss model. In addition, we show the values for $\gamma(\nu)$ for two spheres with a closed membrane neck of initial spherical volume V_s for a single sphere of half the initial volume V_s and for a single sphere of volume V_s (solid purple line). In contrast to the full model (Fig. 5), we find that in the simple loss model, the gain/loss factor γ
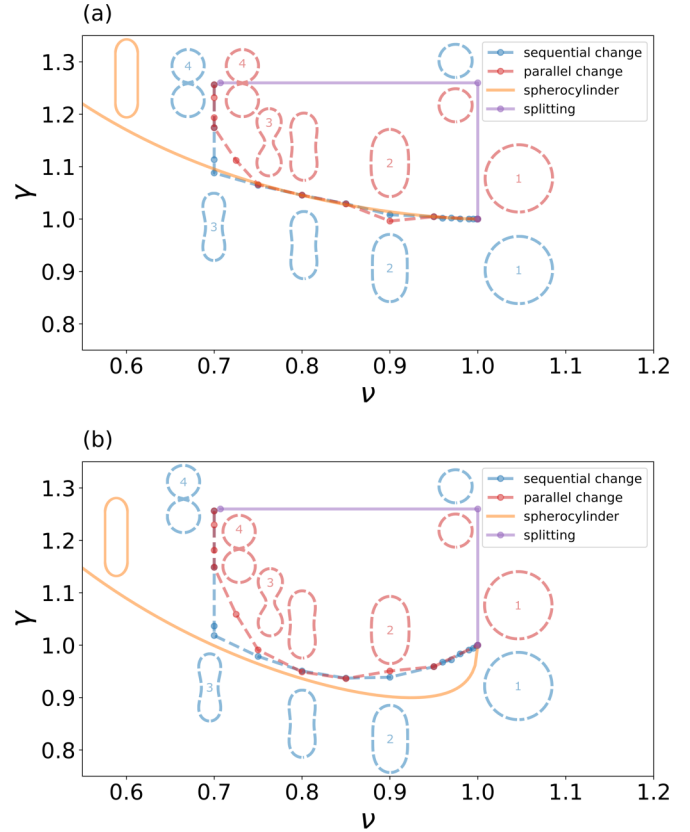

FIG. 6. Membrane turnover during division for the simple loss model (a) and the simple gain model (b). We plot $\gamma(\nu)$ for the sequential change sequence (dashed blue line) and parallel change (dashed red line). The corresponding membrane shapes from Fig. 2 are plotted along the curves in the corresponding colors. In orange, we plot $\gamma(\nu)$ for a spherocylinder of increasing length. In purple, the analytical values are shown for two connected spheres, a small sphere and a large sphere.

monotonically increases during splitting. Thus, for a constant exocytotic activity, the endocytotic activity is at minimum just before division starts and increases until division is complete.

In Fig. 6(b), we plot the same as in Fig. 6(a) but now for the simple gain model. In this case, we find that the gain/loss factor γ nonmonotonically changes during splitting, qualitatively similar to Fig. 5. We therefore conclude that the nonmonotonic change of γ results from the curvature contribution in the loss term in Eq. (3).

V. DISCUSSION

The ability to reproduce is one of the basic requirements that every living being must fulfill. Replication is achieved through division at the cellular level. During cell division at constant volume, the cell shape changes drastically. The change of shape requires a gain of projected area, which is regulated by the total membrane area and driven through membrane trafficking. However, it is still unclear how membrane gain and loss must adapt to membrane deformations during cytokinesis [34]. In this paper, we have developed a kinetic model for membrane trafficking that is based on the membrane shape. To represent the cell shape in our model,

we use FUV shapes as a proxy for cell shapes. This is possible because the shapes of dividing FUVs and cells are relatively similar, although the vesicle shape is determined by membrane energy and the cell shape is determined by the actomyosin cortex [22]. In this way, we can predict how membrane trafficking must adapt to be compatible with membrane deformations during cytokinesis.

To obtain the quasiequilibrium shapes of a dividing FUV, we solved the shape equations of axisymmetric membrane vesicles. In this case, division is driven through decreasing the reduced volume and increasing the preferred curvature. We then formulated a kinetic model for the total membrane area that balances membrane gain and loss, controlled through internal and cell membrane tension and the mean curvature of the projected area of the FUV. By using the sequence of equilibrium FUV shapes on the membrane balance equation at the steady state, we determined how the gain/loss factor (the ratio of kinetic turnover parameters) changes during cell division. We found that the change of the gain/loss factor is determined by the dependence of exocytosis and endocytosis on membrane curvature. The predicted change of the gain/loss factor characterizes the activity of the cell as a result of exo- and endocytosis and demonstrates how membrane trafficking might be regulated and fine-tuned during shape changes. The prediction is in qualitative agreement with the experimental results that suggest that the ratio of exocytosis and endocytosis changes during cell division [14–16].

It has been suggested theoretically that the shape of lipid bilayer vesicles is given by their minimal energy configuration [35,39,58]. Moreover, it has been shown that by increasing the preferred curvature and decreasing the reduced volume, vesicles can get divided [30,32]. Our work starts from similar shapes but goes conceptually one step further. We use vesicle shapes as a proxy for dividing cell shapes and then predict how increasing the projected area of these vesicles is compatible with ongoing membrane trafficking during cell division. For FUVs, it might even be possible to turn around the interpretation of the results of Fig. 5, since for FUVs the shape of the membrane is given by shape energy minimization. Therefore, it seems possible to induce shape deformations through the total membrane area gain that is maintained by a changed ratio of kinetic turnover parameters and by an increased preferred curvature. This interpretation connects back to the old hypothesis that total membrane area gain could drive cytokinesis [59]. However, we emphasize that such a mechanism might only work for artificial cells or protocells, for which the shape is not determined by the actomyosin cortex [22].

Our results extend previous theoretical work, in which the decrease in reduced volume is a consequence of membrane deformations due to energy minimization [40,60,61] or membrane constriction [37,62]. Our results also qualitatively agree with the theoretical results on the growth of membraneless active droplets [63] and prebiotic vesicles [34], where, similar to our work, membrane growth can trigger shape instabilities.

One of the limitations of our work is that we assume that the total membrane area grows proportionally to the projected area. It remains a theoretical challenge for future work to develop a theory for the interplay between membrane fluctuations and membrane reservoirs beyond quasispherical membrane shapes [64–67]. Such a theory should also account

for membrane trafficking and the associated dissipative frictional forces within the membrane and with the surrounding medium [68].

In general, our model can be interpreted in the way that membrane deformations during cytokinesis change membrane gain and loss processes. Therefore, it would be interesting to see if and how one could manipulate cell division by affecting biochemically or physically the gain and loss processes and membrane tensions. Experimentally, for artificial cells, membrane growth was shown to work *in vitro* via vesicle fusion [69,70] or within liposomes via lipid synthesis [71]. In combination with volume conservation and increased preferred curvature, we suggest that these techniques could be tested in the future for their potential to drive vesicle fission.

APPENDIX A: SHAPE EQUATIONS FOR LIPID VESICLES

To calculate vesicle shapes from Eq. (1), we closely follow the procedure as outlined in Ref. [40], which we briefly summarize in the following.

1. Vesicle parametrization

We consider a vesicle of axisymmetric shape around the z axis and parametrize the shape as a function of the arc length s from the south pole ($s = 0$) to the north pole ($s = s_{\max}$). At every arc length s, the shape is then completely described by the distance $\rho(s)$ to the z axis and the tilt angle $\psi(s)$, which is the angle between the horizontal ρ axis and a tangent to the contour at arc length s. Given this parametrization, the two principle curvatures of the vesicle shape read $C_1 = d\psi/ds = \psi'(s) = u(s)$ and $C_2 = \sin\psi/\rho$. The mean curvature reads $H = (\psi'(s) + \sin(\psi)/\rho)/2$.

2. Nondimensionalized shape equations

Minimizing the membrane energy, as defined in Eq. (1), is equivalent to solving the Euler-Lagrange equations, for which the corresponding Lagrange function in the parametrization of an axisymmetric vesicle reads

$$\mathcal{L}(\psi, \psi', \rho, \rho', \zeta) = \frac{\rho}{2}\left(\psi' + \frac{\sin\psi}{\rho} - 2H_0\right)^2 - \frac{\Delta P}{2\kappa}\rho^2\sin\psi + \frac{\Sigma}{\kappa}\rho + \zeta(\rho' - \cos\psi), \tag{A1}$$

where the last term includes the geometric constraint $\rho' = \cos\psi$ by means of the Lagrange multiplier ζ. The shape energy reads in this parametrization

$$\mathcal{H} = 2\pi\kappa \int_0^{s_{\max}} ds\, \mathcal{L}(\psi, \psi', \rho, \rho', \zeta). \tag{A2}$$

From Eq. (A2), we obtain the shape equations as Euler-Lagrange equations. We directly write them in

nondimensionalized form together with the differential equations for the partial area and volume,

$$\frac{d\bar{\rho}}{d\bar{s}} = \mho \cos \bar{\psi}, \tag{A3}$$

$$\frac{d\bar{\psi}}{d\bar{s}} = \mho \bar{u}, \tag{A4}$$

$$\frac{d\bar{u}}{d\bar{s}} = \mho \left(\frac{\sin \bar{\psi} \cos \bar{\psi}}{\bar{\rho}^2} - \frac{\cos \bar{\psi}}{\bar{\rho}} \bar{u} - \frac{1}{2} \Delta \bar{P} \bar{\rho} \cos \bar{\psi} + \frac{\sin \bar{\psi}}{\bar{\rho}} \bar{\zeta} \right), \tag{A5}$$

$$\frac{d\bar{\zeta}}{d\bar{s}} = \mho$$
$$\times \left(\frac{1}{2} (\bar{u} - 2\bar{H}_0)^2 - \frac{\sin^2 \bar{\psi}}{2\bar{\rho}^2} - \Delta \bar{P} \bar{\rho} \sin \bar{\psi} + \bar{\Sigma} \right), \tag{A6}$$

$$\frac{d\Delta \bar{A}}{d\bar{s}} = \frac{\mho}{2} \bar{\rho}, \tag{A7}$$

$$\frac{d\Delta \bar{V}}{d\bar{s}} = \frac{3\mho}{4} \bar{\rho}^2 \sin \bar{\psi}, \tag{A8}$$

with the following nondimensionalized quantities that are expressed by the vesicle radius $R_{ve} = \sqrt{A/(4\pi)}$:

$$\bar{s} = \frac{s}{s_{\max}}, \tag{A9}$$

$$\bar{\rho}(\bar{s}) = \frac{\rho(s)}{R_{ve}}, \tag{A10}$$

$$\bar{u}(\bar{s}) = R_{ve} u(s), \tag{A11}$$

$$\bar{\zeta}(\bar{s}) = R_{ve} \zeta(s), \tag{A12}$$

$$\bar{\psi}(\bar{s}) = \psi(s), \tag{A13}$$

$$\mho = \frac{s_{\max}}{R_{ve}}, \tag{A14}$$

$$\Delta \bar{P} = \Delta P \frac{R_{ve}^3}{\kappa}, \tag{A15}$$

$$\bar{\Sigma} = \Sigma \frac{R_{ve}^2}{\kappa}, \tag{A16}$$

$$\Delta \bar{A}(\bar{s}) = \frac{\Delta A(s)}{4\pi R_{ve}^2} = \frac{2\pi \int_0^s ds' \rho(s')}{4\pi R_{ve}^2}$$
$$= \frac{\mho}{2} \int_0^{\bar{s}} d\bar{s}' \bar{\rho}(\bar{s}'), \tag{A17}$$

$$\Delta \bar{V}(\bar{s}) = \frac{\Delta V(s)}{\frac{4\pi}{3} R_{ve}^3} = \frac{\pi \int_0^s ds \, \rho^2(s') \sin \psi(s')}{\frac{4\pi}{3} R_{ve}^3} \tag{A18}$$
$$= \frac{3\mho}{4} \int_0^{\bar{s}} d\bar{s}' \bar{\rho}^2(\bar{s}') \sin \bar{\psi}(\bar{s}'). \tag{A19}$$

3. Boundary conditions and regularization close to the south and north pole:

Equations (A3)–(A8) are subject to the following boundary conditions in nondimensionalized form:

$$\bar{\rho}(\bar{s} = 0) = 0 \quad \text{and} \quad \bar{\rho}(\bar{s} = 1) = 0, \tag{A20}$$

$$\bar{\psi}(\bar{s} = 0) = 0 \quad \text{and} \quad \bar{\psi}(\bar{s} = 1) = \pi, \tag{A21}$$

$$\bar{u}(\bar{s} = 0) = \bar{U}_0 \quad \text{and} \quad \bar{u}(\bar{s} = 1) = \bar{U}_1, \tag{A22}$$

$$\bar{\zeta}(\bar{s} = 0) = 0 \quad \text{and} \quad \bar{\zeta}(\bar{s} = 1) = 0, \tag{A23}$$

$$\Delta \bar{A}(\bar{s} = 0) = 0 \quad \text{and} \quad \Delta \bar{A}(\bar{s} = 1) = 1, \tag{A24}$$

$$\Delta \bar{V}(\bar{s} = 0) = 0 \quad \text{and} \quad \Delta \bar{V}(\bar{s} = 1) = \nu, \tag{A25}$$

with $\bar{U}_0 = U_0 R_{ve} = u(s = 0)R_{ve}$ and $\bar{U}_1 = U_1 R_{ve} = u(s = s_{\max})R_{ve}$. To solve Eqs. (A3)–(A8), subject to the boundary conditions as defined in Eqs. (A20)–(A25), we use the shooting algorithm. However, during the numerical integration of the shape Eqs. (A3)–(A8), one faces instabilities around $\bar{\rho} = 0$. Therefore, to avoid numerical instabilities, one can Taylor expand Eqs. (A3)–(A8) around the south pole ($\bar{s} = 0$) and the north pole ($\bar{s} = 1$) and match the expansion with the numerical integration.

4. Expansion around the south pole

Close to the south pole ($\bar{s} = 0$), the expansion reads in nondimensionalized form

$$\bar{\rho} = \bar{\rho}_1 \bar{s} + \frac{1}{6} \bar{\rho}_3 \bar{s}^3 + ..., \tag{A26}$$

$$\bar{\psi} = \bar{\psi}_1 \bar{s} + \frac{1}{6} \bar{\psi}_3 \bar{s}^3 + ..., \tag{A27}$$

$$\bar{u} = \bar{U}_0 + \frac{1}{2} \frac{\bar{\psi}_3}{\mho} \bar{s}^2 + ..., \tag{A28}$$

$$\bar{\zeta} = \bar{\zeta}_1 \bar{s} + \frac{1}{6} \bar{\zeta}_3 \bar{s}^3 + ..., \tag{A29}$$

$$\Delta \bar{A} = \frac{\mho^2}{4} \bar{s}^2 - \frac{\mho^4}{48} \bar{s}^4 + ..., \tag{A30}$$

$$\Delta \bar{V} = \frac{3\mho^4}{16} \bar{s}^4 + ..., \tag{A31}$$

with the coefficients

$$\bar{\rho}_1 = \mho \quad \text{and} \quad \bar{\rho}_3 = -\mho^3 \bar{U}_0^2, \tag{A32}$$

$$\bar{\psi}_1 = \mho \bar{U}_0 \quad \text{and}$$
$$\bar{\psi}_3 = \frac{3\mho^3}{8} (4\bar{H}_0 \bar{U}_0 (\bar{H}_0 - \bar{U}_0) - \Delta \bar{P} + 2\bar{U}_0 \bar{\Sigma}), \tag{A33}$$

$$\bar{\zeta}_1 = \mho (2\bar{H}_0 (\bar{H}_0 - \bar{U}_0) + \bar{\Sigma}) \quad \text{and}$$
$$\bar{\zeta}_3 = \mho^3 \left(\bar{H}_0 \bar{U}_0 (\bar{H}_0 - \bar{U}_0)(\bar{U}_0 - 3\bar{H}_0) - \frac{3}{4} (3\bar{U}_0 - \bar{H}_0) \Delta \bar{P} \right)$$
$$+ \mho^3 \left(\frac{1}{2} \bar{U}_0 (\bar{U}_0 - 3\bar{H}_0) \bar{\Sigma} \right). \tag{A34}$$

5. Expansion around the north pole

Close to the north pole ($\bar{s} = 1$), the expansion, in nondimensionalized form with $\bar{\epsilon} = 1 - \bar{s}$, reads

$$\bar{\rho}^{no} = \bar{\rho}_1^{no} \bar{\epsilon} + \frac{1}{6} \bar{\rho}_3^{no} \bar{\epsilon}^3 + ..., \tag{A35}$$

$$\bar{\psi}^{no} = \bar{\psi}_1^{no} \bar{\epsilon} + \frac{1}{6} \bar{\psi}_3^{no} \bar{\epsilon}^3 + ..., \tag{A36}$$

$$\bar{u}^{\text{no}} = \bar{U}_1 + \frac{1}{2}\frac{\bar{\psi}_3^{\text{no}}}{\mho}\bar{\epsilon}^2 + ..., \tag{A37}$$

$$\bar{\zeta}^{\text{no}} = \bar{\zeta}_1^{\text{no}}\bar{\epsilon} + \frac{1}{6}\bar{\zeta}_3^{\text{no}}\bar{\epsilon}^3 + ..., \tag{A38}$$

$$\bar{A}^{\text{no}} = 1 - \frac{\mho^2}{4}\bar{\epsilon}^2 + \frac{\mho^4}{48}\bar{U}_1^2\bar{\epsilon}^4 + ..., \tag{A39}$$

$$\bar{V}^{\text{no}} = \nu - \frac{\mho^4}{16}\bar{U}_1\bar{\epsilon}^4 + ..., \tag{A40}$$

with the coefficients

$$\bar{\rho}_1^{\text{no}} = \mho \quad \text{and} \quad \bar{\rho}_3^{\text{no}} = -\mho^3\bar{U}_1^2, \tag{A41}$$

$\bar{\psi}_1^{\text{no}} = \mho\bar{U}_1$ and

$$\bar{\psi}_3^{\text{no}} = \frac{3\mho^3}{8}(4\bar{H}_0\bar{U}_1(\bar{H}_0 - \bar{U}_1) - \Delta\bar{P} + 2\bar{U}_1\bar{\Sigma}), \tag{A42}$$

$\bar{\zeta}_1^{\text{no}} = \mho(2\bar{H}_0(\bar{U}_1 - \bar{H}_0) - \bar{\Sigma})$ and

$$\bar{\zeta}_3^{\text{no}} = \mho^3\left(\bar{H}_0\bar{U}_1(\bar{H}_0 - \bar{U}_1)(3\bar{H}_0 - \bar{U}_1) + \frac{3}{4}(3\bar{U}_1 - \bar{H}_0)\Delta\bar{P}\right)$$
$$+ \mho^3\left(\frac{1}{2}\bar{U}_1(3\bar{H}_0 - \bar{U}_1)\bar{\Sigma}\right). \tag{A43}$$

6. Numerical implementation

To calculate the membrane shapes for axisymmetric vesicles, we now solve the shape Eqs. (A3)–(A8).

(1) We fix values for the reduced volume ν and the reduced preferred curvature $\bar{H}_0$. For every combination of $(\nu, \bar{H}_0)$, we choose initial values for the five parameters $\mho, \bar{U}_0, \bar{U}_1, \Delta\bar{P}$, and $\bar{\Sigma}$. Next, using Eq. (A26), we calculate a value for $\bar{s}_{\text{n}*}$ so $\bar{\rho}(\bar{s}_{\text{n}*})$ is the smallest value that is larger than the threshold. For this purpose, we choose $\Delta\bar{s} = 10^{-4}$ and iterate positive integers n with $\bar{s}_n = n \cdot \Delta\bar{s}$ until $\bar{\rho}(\bar{s}_{\text{n}*}) > 3.5 \times 10^{-2}$. The value $\bar{s}_{\text{n}*}$ is then chosen as initial arc length $\bar{s}_{\text{ini}} = \bar{s}_{\text{n}*}$.

(2) We calculate initial values for $\bar{\rho}, \bar{\psi}, \bar{u}, \bar{\zeta}, \Delta\bar{A}$, and $\Delta\bar{V}$ by using $\bar{s}_{\text{ini}}$ on Eqs. (A26)–(A31).

(3) Given the chosen initial values for $\mho, \bar{U}_0, \bar{U}_1, \Delta\bar{P}$, and $\bar{\Sigma}$, we integrate the shape Eqs. (A3)–(A8) from the initial values until we reach the final value $\bar{s}_{\text{fin}} = 1 - \bar{s}_{\text{ini}}$ along 1000 data points. For the integration, we use the solve_ivp function from scipy.integrate [72] with the Radau method, which is an implicit Runge-Kutta procedure. From the integration, we obtain six final values for $\bar{\rho}, \bar{\psi}, \bar{u}, \bar{\zeta}, \Delta\bar{A}$, and $\Delta\bar{V}$.

(4) We calculate final values for $\bar{\rho}, \bar{\psi}, \bar{u}, \bar{\zeta}, \Delta\bar{A}$, and $\Delta\bar{V}$ by using $\bar{\epsilon}_{\text{fin}} = 1 - \bar{s}_{\text{fin}}$ on Eqs. (A35)–(A40).

(5) By comparing the final values from the integration of Eqs. (A3)–(A8) to the final values obtained from the expansion through Eqs. (A35)–(A40), we get six residual values $(\bar{\rho}(\bar{s}_{\text{fin}}) - \bar{\rho}^{\text{no}}(\bar{\epsilon}_{\text{fin}}), \bar{\psi}(\bar{s}_{\text{fin}}) - (\pi - \bar{\psi}^{\text{no}}(\bar{\epsilon}_{\text{fin}})), \bar{u}(\bar{s}_{\text{fin}}) - \bar{u}^{\text{no}}(\bar{\epsilon}_{\text{fin}}), \bar{\zeta}(\bar{s}_{\text{fin}}) - \bar{\zeta}^{\text{no}}(\bar{\epsilon}_{\text{fin}}), \Delta\bar{A}(\bar{s}_{\text{fin}}) - \Delta\bar{A}^{\text{no}}(\bar{\epsilon}_{\text{fin}}), \Delta\bar{V}(\bar{s}_{\text{fin}}) - \Delta\bar{V}^{\text{no}}(\bar{\epsilon}_{\text{fin}}))$ that depend on the five (variable) parameters $\mho, \bar{U}_0, \bar{U}_1, \Delta\bar{P}$, and $\bar{\Sigma}$ and on ν and $\bar{H}_0$. To determine the five parameter values of $\mho, \bar{U}_0, \bar{U}_1, \Delta\bar{P}$, and $\bar{\Sigma}$, we minimize the six residuals with the least_squares function from scipy.optimize [72] by using the lm method, which is a Levenberg-Marquardt algorithm. In this way, we determine the parameter values for fixed values of ν and $\bar{H}_0$.

TABLE I. Parameter values for the sequential change sequence in Fig. 2(a). Reduced volume ν, reduced preferred curvature $\bar{H}_0$, spherical vesicle radius R, volume V, projected area A, preferred curvature H_0, reduced area A/A_s, and spherical reduced preferred curvature $\bar{H}_0^s$. To get explicit values, we assume a volume of $V = 4189\,\mu\text{m}^3$, corresponding to a sphere radius of $R = 10\,\mu\text{m}$.

ν	$\bar{H}_0$	$R\,(\mu\text{m})$	$V\,(\mu\text{m}^3)$	$A\,(\mu\text{m}^2)$	$H_0\,(\mu\text{m}^{-1})$	A/A_s	$\bar{H}_0^s$
1.0	0	10	4189	1257	0	1.00	0
0.95	0		4189	1300	0	1.03	0
0.90	0		4189	1348	0	1.07	0
0.85	0		4189	1400	0	1.11	0
0.80	0		4189	1458	0	1.16	0
0.75	0		4189	1522	0	1.21	0
0.70	0		4189	1594	0	1.27	0
0.70	0.5		4189	1594	0.044	1.27	0.44
0.70	1.0		4189	1594	0.089	1.27	0.89
0.70	1.41		4189	1594	0.125	1.27	1.25

APPENDIX B: SUMMARY OF PARAMETER VALUES FOR THE CALCULATED VESICLE SHAPES

In Tables I and II, we calculate the reduced volume ν, the reduced preferred curvature $\bar{H}_0$, the spherical vesicle radius R, the volume V, the projected area A, the preferred curvature H_0, the reduced area A/A_s, and the spherical reduced preferred curvature $\bar{H}_0^s$ for the sequential and parallel change sequence in Figs. 2(a) and 2(b).

APPENDIX C: STABILITY OF THE AREA BALANCE EQUATION WITH RESPECT TO SIZE DEFORMATIONS

In this Appendix, we investigate the stability of the area balance equation, as formulated in Eq. (3), with respect to size deformations. We show that besides the clear phenomenological motivation of Eq. (2), the deduced Eq. (3) is also meaningful from a geometrical perspective. Since both total membrane area gain and loss depend on membrane curvature, giving rise to geometrical feedback and a dynamic balance

TABLE II. Parameter values for the parallel change sequence in Fig. 2(b). Reduced volume ν, reduced preferred curvature $\bar{H}_0$, spherical vesicle radius R, volume V, projected area A, preferred curvature H_0, reduced area A/A_s, and spherical reduced preferred curvature $\bar{H}_0^s$. To get explicit values, we assume a volume of $V = 4189\,\mu\text{m}^3$, corresponding to a sphere radius of $R = 10\,\mu\text{m}$.

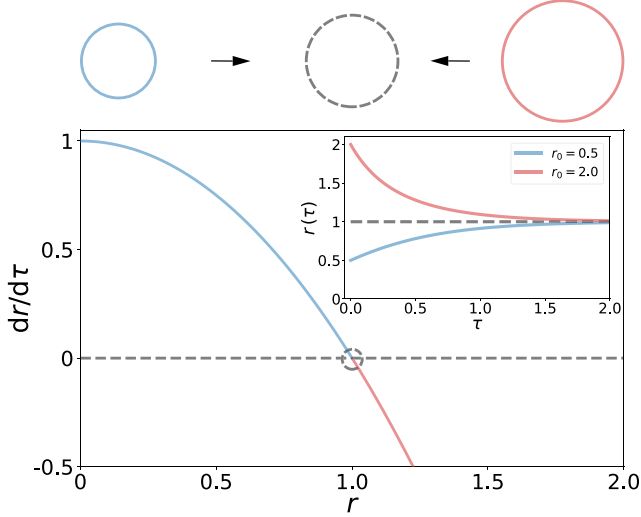| ν	$\bar{H}_0$	$R\,(\mu\text{m})$	$V\,(\mu\text{m}^3)$	$A\,(\mu\text{m}^2)$	$H_0\,(\mu\text{m}^{-1})$	A/A_s	$\bar{H}_0^s$
1.0	0	10	4189	1257	0	1.00	0
0.95	0.17		4189	1300	0.017	1.03	0.17
0.90	0.33		4189	1348	0.032	1.07	0.32
0.85	0.50		4189	1400	0.047	1.11	0.47
0.80	0.67		4189	1458	0.062	1.16	0.62
0.75	0.83		4189	1522	0.075	1.21	0.75
0.70	1.0		4189	1594	0.089	1.27	0.89
0.70	1.1		4189	1594	0.098	1.27	0.98
0.70	1.3		4189	1594	0.115	1.27	1.15
0.70	1.41		4189	1594	0.125	1.27	1.25

FIG. 7. Effect of the area balance equation on the projected area. The change of the non-dimensionalized sphere radius $dr/d\tau$ is plotted as a function of the sphere radius r. With curvature dependent kinetic turnover parameters, $dr/d\tau$ is positive for $r < 1$ (blue line) and negative for $r > 1$ (red line), predicting a single stable steady state at $r = 1$ (gray circle). Inset: The stable solutions of $r(\tau)$ for different initial radii r_0 (blue and red line). Top: For initial radii $r > 1$, the sphere shrinks (red). For initial radii $r < 1$, the sphere grows (blue), leading to one stable sphere size (gray) at $r = 1$.

mechanism [73], we expect to find a steady state of the total membrane area. To illustrate this idea, we assume a homogenous area density β, so the total membrane area and the projected area are proportional to each other. For simplicity, we then set $\beta = 1$, effectively neglecting the difference between total membrane area and projected area. Moreover, we consider a spherical cell with radius R, and projected area $A = 4\pi R^2$. Simplifying and nondimensionalizing Eq. (3) yields $dr/d\tau = 1 - r^2$, with the steady-state radius $R_s = \sqrt{k_{on}/k_{off}}$ and the nondimensionalized radius $r = R/R_s$ and time $\tau = t\sqrt{k_{on}k_{off}}/2$. Alternatively, the steady-state radius can be converted into the spherical area $A_s = 4\pi k_{on}/k_{off}$. This result also suggests an interpretation of the ratio k_{on}/k_{off}: For any shape, there is a value for this ratio, corresponding to an area, for which the area balance equation is at steady state. Fig. 7 shows the change of the sphere radius $dr/d\tau$ as a function of r (blue line). $dr/d\tau$ switches from positive to negative values with increasing values of r and vanishes for $r = 1$, corresponding to a stable steady state. The equation is solved by $r(\tau) = (r_0(1 + e^{2\tau}) - (1 - e^{2\tau}))/(-r_0(1 - e^{2\tau}) + (1 + e^{2\tau}))$, as plotted in the inset of Fig. 7 for two values of the initial size r_0 (red and blue line). Independent of the initial value of r_0, the steady-state area is fully determined by k_{on} and k_{off}.

The stability behavior of the steady states for a spherical shape can be generalized to the case that both kinetic turnover parameters scale with the same power of H, which is $k_{on}H^\alpha$ and k_{off}/H^α. In general, we find a steady state at $R_s = (k_{on}/k_{off})^{1/(2\alpha)}$ that is stable for $\alpha > 0$ and unstable for $\alpha < 0$. For $|\alpha| < 1$, another steady state appears at $R_s = 0$, which is unstable if $\alpha > 0$ and stable if $\alpha < 0$. For $\alpha = 0$, no steady state exists (except $R_s = 0$) since we only find

exponential growth or decay depending on k_{on} and k_{off}. Thus, a modified area balance equation with curvature independent area gain and loss terms ($\alpha = 0$) would not lead to a stable cell size. We note that our choice of $\alpha = 1$ is not special, but only convenient.

To conclude, Eq. (3) defines an area balance equation that is both phenomenologically and geometrically reasonable and leads to finite and stable membrane areas for spherical shapes.

APPENDIX D: STABILITY OF THE AREA BALANCE EQUATION WITH RESPECT TO SHAPE DEFORMATIONS

In this Appendix, we investigate the stability of the area balance equation, as formulated in Eq. (3), with respect to shape deformations. We assume that the volume is constant and independently controlled from the projected membrane area. Under this assumption, we investigate whether shapes that are deviating from the spherical shape can be stable and whether the spherical shape can get destabilized by changing k_{on} and k_{off}. Because we are only interested in the stability behavior of Eq. (3), we neglect the distinction between total membrane area and projected area within this section. We investigate the stability of shapes that can be expressed by small deformations of the spherical shape. Therefore, we perturb a spherical shape by expanding the radius R around the radius of a sphere R_s as a function of the azimuthal angle θ and polar angle ϕ, with a small generic deformation $u(\theta, \phi)$. We obtain, with the notation of Ref. [74], $R(\theta, \phi, t) = R_s + u(\theta, \phi, t) = R_s(1 + f(\theta, \phi, t))$, where $f(\theta, \phi, t) = u(\theta, \phi, t)/R_s$ determines the relative deformation and $\boldsymbol{R} = R(\theta, \phi, t)\boldsymbol{e}_r$ points in the direction of $\boldsymbol{e}_r$.

To calculate the integrals in Eq. (3) we follow [66,74–76] and expand the mean curvature H, the inverse mean curvature $1/H$, the area element dA, the area change $\dot{A}$, and volume element dV up to second order in f, assuming small deformations. We then express f in terms of the spherical harmonics, $f(\theta, \phi, t) = \sum_{l,m} f_{lm}(t)Y_{lm}(\theta, \phi)$, and calculate all terms of Eq. (3).

In detail, we first define the normal vector:

$$\hat{\boldsymbol{n}} = \frac{\frac{\partial \boldsymbol{R}}{\partial \theta} \times \frac{\partial \boldsymbol{R}}{\partial \phi}}{\left|\frac{\partial \boldsymbol{R}}{\partial \theta} \times \frac{\partial \boldsymbol{R}}{\partial \phi}\right|}. \tag{D1}$$

The mean curvature, expanded up to second order in f, is given by [74]

$$H = \frac{1}{2}\nabla \cdot \hat{\boldsymbol{n}} \approx \frac{1}{R_s}\left(1 - f - \frac{1}{2}\Delta_2 f + f^2 + f\Delta_2 f\right), \tag{D2}$$

with

$$\Delta_2 = \frac{1}{\sin\theta}\frac{\partial}{\partial\theta}\left(\sin\theta\frac{\partial}{\partial\theta}\right) + \frac{1}{\sin^2\theta}\frac{\partial^2}{\partial\phi^2}. \tag{D3}$$

The infinitesimal area element is also expanded up to second order in f [74],

$$dA = \sqrt{\det g}\,d\theta d\phi \approx R_s^2\left(1 + 2f + f^2 + \tfrac{1}{2}(\nabla_2 f)^2\right)d\Omega, \tag{D4}$$

where $\det g$ is the determinant of the metric tensor $g_{ij} = \boldsymbol{R}_{,i} \cdot \boldsymbol{R}_{,j}$, $\{i, j\} = \{\theta, \phi\}$, $d\Omega = \sin\theta d\theta d\phi$ is the infinitesimal solid

angle element, and

$$\boldsymbol{\nabla}_2 = \left(\frac{\partial}{\partial \theta}, \frac{1}{\sin \theta} \frac{\partial}{\partial \phi} \right). \tag{D5}$$

The infinitesimal volume element can be expressed by means of the divergence theorem and expanded up to second order in f [75,76]:

$$dV = \frac{1}{3} \hat{\boldsymbol{n}} \cdot \boldsymbol{R} \, dA = \frac{1}{3} R^3 \, d\Omega \approx \frac{R_s^3}{3} (1 + 3f + 3f^2) \, d\Omega. \tag{D6}$$

Next, we expand $f(\theta, \phi, t)$ in spherical harmonics,

$$f(\theta, \phi, t) = \sum_{l=0}^{l_{\max}} \sum_{m=-l}^{l} f_{lm}(t) Y_{lm}(\theta, \phi), \tag{D7}$$

where Y_{lm} are the spherical harmonic functions and f_{lm} are the corresponding amplitudes for which we have $f_{lm}^* = (-1)^m f_{l-m}$ [66]. We introduce a cutoff $l_{\max} \propto R_s/d$ [66], with R_s the cell size of around 500 nm–50 μm and d the membrane thickness of several nanometers.

We recapitulate several relations that are used in the following to calculate the different integrals that occur in Eq. (3) [74]:

$$\Delta_2 Y_{lm} = -l(l+1) Y_{lm},$$

$$\int f \, d\Omega = \sqrt{4\pi} f_{00},$$

$$\int f^2 \, d\Omega = \sum_l \sum_m |f_{lm}|^2,$$

$$\int (\boldsymbol{\nabla}_2 f)^2 \, d\Omega = -\int f \Delta_2 f \, d\Omega. \tag{D8}$$

First, we calculate the volume:

$$V = \frac{4\pi}{3} R_s^3 \left(\left(1 + \frac{f_{00}}{\sqrt{4\pi}} \right)^3 + \frac{3}{4\pi} \sum_{l>0} \sum_m |f_{lm}|^2 \right). \tag{D9}$$

Assuming volume conservation, $V = \frac{4\pi}{3} R_s^3$, we can relate the first amplitude to the sum of all other amplitudes:

$$f_{00} = -\frac{1}{\sqrt{4\pi}} \sum_{l>0} \sum_m |f_{lm}|^2. \tag{D10}$$

Using Eq. (D10), the total area reads

$$A = R_s^2 \left[4\pi + 2\sqrt{4\pi} f_{00} + \sum_{l=0} \sum_m \left(1 + \frac{1}{2} l(l+1) \right) |f_{lm}|^2 \right]$$

$$= 4\pi R_s^2 \left[1 + \frac{1}{4\pi} \sum_{l>1} \sum_m \frac{1}{2} (l+2)(l-1) |f_{lm}|^2 \right]$$

$$= 4\pi R_s^2 \left[1 + \frac{1}{4\pi} \sum_{l>1} \sum_m \lambda |f_{lm}|^2 \right], \tag{D11}$$

where $\lambda = (l+2)(l-1)/2$. The change in area is thus

$$\dot{A} = R_s^2 \sum_{l>1} \sum_m \lambda (\dot{f}_{lm} f_{lm}^* + f_{lm} \dot{f}_{lm}^*)$$

$$= 2R_s^2 \sum_{l>1} \sum_m \lambda f_{lm} \dot{f}_{lm}^* = 2R_s^2 \sum_{l>1} \sum_m \lambda \dot{f}_{lm} f_{lm}^*, \tag{D12}$$

where we used that $f_{lm}^* = (-1)^m f_{l-m}$ and an index shift from m to $-m$. Next, we calculate the first term on the right-hand side of Eq. (3),

$$H \, dA \approx R_s \left(1 + f - \frac{1}{2} \Delta_2 f + \frac{1}{2} (\boldsymbol{\nabla}_2 f)^2 \right) d\Omega, \tag{D13}$$

and therefore

$$\int H \, dA = 4\pi R_s \left(1 + \frac{1}{4\pi} \sum_{l>1} \sum_m \lambda |f_{lm}|^2 \right). \tag{D14}$$

Furthermore, we have

$$\frac{1}{H} \, dA \approx R_s^3 \, d\Omega \left(1 + 3f + 3f^2 + \frac{1}{2} \Delta_2 f + f \Delta_2 f \right.$$

$$\left. + \frac{1}{2} (\boldsymbol{\nabla}_2 f)^2 + \frac{1}{4} (\Delta_2 f)^2 \right), \tag{D15}$$

and thus

$$\int \frac{1}{H} \, dA = 4\pi R_s^3 \left(1 + \frac{1}{8\pi} \sum_{l>1} \sum_m l(l+1) \lambda |f_{lm}|^2 \right). \tag{D16}$$

Using these relations on Eq. (3), we obtain

$$\sum_{l>1} \sum_m \lambda f_{lm} \dot{f}_{lm}^* = \sum_{l>1} \sum_m \lambda \dot{f}_{lm} f_{lm}^*$$

$$= \frac{k_{\mathrm{on}}}{2R_s} \left[4\pi (1 - \gamma) + \sum_{l>1} \sum_m \lambda |f_{lm}|^2 \right]$$

$$- \frac{k_{\mathrm{on}}}{2R_s} \left[\frac{\gamma}{2} \sum_{l>1} \sum_m l(l+1) \lambda |f_{lm}|^2 \right], \tag{D17}$$

with $\lambda = (l+2)(l-1)/2$. Moreover, we assume that the spherical steady-state kinetic turnover parameters k_{on}^s and k_{off}^s determine the initial sphere radius $R_s = \sqrt{k_{\mathrm{on}}^s/k_{\mathrm{off}}^s}$. Then, we can introduce the gain/loss factor (the ratio of kinetic turnover parameters between the initial and the current membrane gain and loss) $\gamma = R_s^2 k_{\mathrm{off}}/k_{\mathrm{on}} = (k_{\mathrm{on}}^s k_{\mathrm{off}})/(k_{\mathrm{on}} k_{\mathrm{off}}^s)$. We note that when plugging in the definition of k_{on} and k_{off}, we find an alternative meaning of $\gamma = (\Gamma_{\mathrm{cm}}^s \Gamma_{\mathrm{i}})/(\Gamma_{\mathrm{i}}^s \Gamma_{\mathrm{cm}})$ that is the ratio of membrane tensions.

Equation (D17) determines the time evolution of the deformation amplitudes f_{lm} as a function of γ. In general, Eq. (D17) is expected to only hold true close to the spherical shape and does not yet specify any particular shape. To analyze the stability behavior of Eq. (D17), we thus have to choose particular shapes. First, we observe that division defines an axis around which the system has rotational symmetry. Identifying this axis with the z axis of the spherical harmonics, the only modes that obey this rotational symmetry are the ones with $m = 0$. Since $m = 0$, the spherical harmonics and the amplitudes f_{l0} are real valued. We note that when assuming rotational symmetry, it is possible to expand Eq. (3) directly in Legendre polynomials [38,77]. Moreover, for simplicity, we choose to analyze the stability behavior of shapes that are fully described by the first mode ($l = 2$). We note that other choices are possible as well. Then, we can replace the sums in Eq. (D17) by the contribution from the prolate mode ($l = 2, m = 0$) and rewrite the equation.
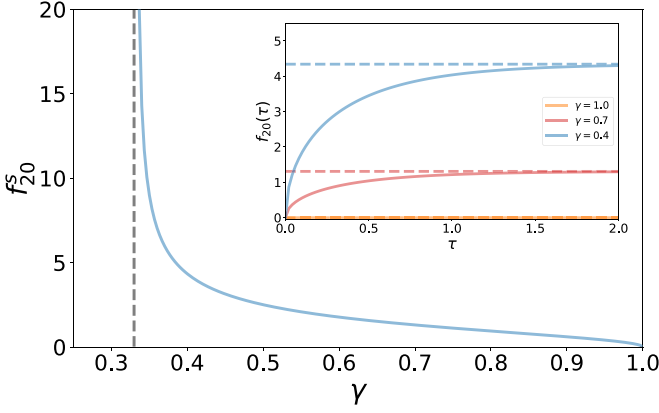
FIG. 8. The steady-state amplitude f_{20}^{s} as a function of γ according to Eq. (D19). For $\gamma = 1$, the amplitude vanishes and the spherical shape is restored. For $\gamma = 1/3$, the amplitude diverges. For $1/3 < \gamma < 1$, the amplitude is finite, so the spherical shape is destabilized and stable shapes develop. Inset: Time evolution of $f_{20}(\tau)$ for different values of γ.

From Eq. (D17), we then find a nondimensionalized equation for the amplitude f_{20},

$$\frac{df_{20}}{d\tau} = \frac{2\pi(1-\gamma)}{3\gamma - 1} \frac{1}{f_{20}} - f_{20}, \tag{D18}$$

with the nondimensionalized time $\tau = t\sqrt{k_{\mathrm{on}}k_{\mathrm{off}}}(3\gamma - 1)/(2\sqrt{\gamma})$. We solve Eq. (D18) with the initial condition $f_{20}(\tau = 0) = 0$ and get

$$f_{20} = f_{20}^{\mathrm{s}}\sqrt{1 - e^{-2\tau}}. \tag{D19}$$

For $\tau \to \infty$, the steady-state amplitude is given by $f_{20}^{\mathrm{s}} = \sqrt{2\pi(1-\gamma)/(3\gamma - 1)}$. Figure 8 shows the steady-state amplitude of Eq. (D19) as a function of γ. While for $\gamma = 1$ the amplitude vanishes, indicating that the shape stays spherical, for $\gamma = 1/3$ the amplitude diverges, indicating that the model assumption of small deformations breaks down. In between, for $1/3 < \gamma < 1$, the amplitude is finite, implying that the spherical shape is destabilized. We note that for $\gamma \geqslant 1$ the amplitude decays to zero and the spherical shape is stable, whereas for $\gamma \leqslant 1/3$ the amplitude explodes and the shape is completely destabilized. Thus, we consider Eq. (D17) in the case where $1/3 < \gamma \leqslant 1$, that is, for a moderate change of the membrane gain or loss processes, respectively.

The inset of Fig. 8 shows the time evolution of the amplitude according to Eq. (D19). We note that both the timescale for approaching the steady state and the steady-state amplitude depend on γ. To conclude, we find, as expected, that the shape changes for which Eq. (3) is at the steady state because of the gain in total membrane area.

Finally, we relate the steady-state amplitude for the prolate mode ($l = 2$, $m = 0$), defined through Eq. (D19), to the reduced volume. In this way, we obtain a relationship between the kinetic turnover parameter for membrane gain and loss and the membrane shape. We express the projected area in spherical harmonics and use the steady state amplitude, determined

by Eq. (D19). The reduced volume v as a function of γ then reads

$$v(\gamma) = \frac{1}{\left(1 + \frac{1}{3}\left(\frac{1-\gamma}{\gamma - \frac{1}{3}}\right)\right)^{3/2}}. \tag{D20}$$

In Fig. 5, we plot γ as function of v for the the numerically inverted Eq. (D20) (green solid line). It is also straightforward to calculate membrane shapes from the expansion in spherical harmonics close to the sphere by $R(\theta, \phi, \gamma)/R_{\mathrm{s}} = 1 + f_{20}^{\mathrm{s}}Y_{20}$. The resulting shape for $v = 0.95$ is shown along the green line in Fig. 5.

APPENDIX E: ALTERNATIVE AREA BALANCE EQUATIONS

In this Appendix, we study two variants of the area balance equation, defined through Eq. (3). First, we neglect the curvature dependence of the membrane loss term in Eq. (3) and get the simple loss model:

$$\dot{\mathbb{A}} = k_{\mathrm{on}}\int H \, dA - k_{\mathrm{off}}A. \tag{E1}$$

In this case, k_{on} carries the units of a velocity and k_{off} of a rate. Similar to Appendix C, we calculate the steady-state radius for a sphere $R_{\mathrm{s}} = k_{\mathrm{on}}^{\mathrm{s}}/k_{\mathrm{off}}^{\mathrm{s}}$. At steady state, Eq. (E1) reads

$$\frac{k_{\mathrm{off}}}{k_{\mathrm{on}}} = \frac{\int H \, dA}{A}. \tag{E2}$$

Finally, with the definition of γ, we find

$$\gamma = \frac{k_{\mathrm{on}}^{\mathrm{s}}}{k_{\mathrm{off}}^{\mathrm{s}}}\frac{k_{\mathrm{off}}}{k_{\mathrm{on}}} = v^{\frac{1}{3}}R_{\mathrm{ve}}\frac{\int H \, dA}{A}. \tag{E3}$$

For the spherocylinder, we can calculate $\gamma(AR)$ by using the area and mean curvature. We find

$$\gamma(AR) = \frac{(1 + \frac{3}{4}AR)^{\frac{1}{3}}}{1 + \frac{AR}{2}}\left(1 + \frac{AR}{4}\right). \tag{E4}$$

Second, we neglect the curvature dependence of the membrane gain term in Eq. (3) and get the simple gain model:

$$\dot{\mathbb{A}} = k_{\mathrm{on}}A - k_{\mathrm{off}}\int \frac{1}{H} \, dA. \tag{E5}$$

Now k_{on} carries the unit of a rate and k_{off} carries the units of one over length and time. We find the steady-state radius for the sphere to be $R_{\mathrm{s}} = k_{\mathrm{on}}^{\mathrm{s}}/k_{\mathrm{off}}^{\mathrm{s}}$. At the steady state, the simple gain model, defined through Eq. (E5), reads

$$\frac{k_{\mathrm{off}}}{k_{\mathrm{on}}} = \frac{A}{\int \frac{1}{H} \, dA}. \tag{E6}$$

Using the definition of γ, we find

$$\gamma = \frac{k_{\mathrm{on}}^{\mathrm{s}}}{k_{\mathrm{off}}^{\mathrm{s}}}\frac{k_{\mathrm{off}}}{k_{\mathrm{on}}} = v^{\frac{1}{3}}R_{\mathrm{ve}}\frac{A}{\int \frac{1}{H} \, dA}. \tag{E7}$$

For the spherocylinder, we can calculate $\gamma(AR)$ by using the area and mean curvature. We find

$$\gamma(AR) = \frac{(1 + \frac{3}{4}AR)^{\frac{1}{3}}}{1 + AR}\left(1 + \frac{AR}{2}\right). \tag{E8}$$

[1] B. Alberts, A. Johnson, J. Lewis, D. Morgan, M. Raff, K. Roberts, and P. Walter, *Molecular Biology of the Cell*, 6th ed. (Garland Science, New York, 2015)

[2] R. A. Green, E. Paluch, and K. Oegema, Cytokinesis in Animal Cells, Annu. Rev. Cell Dev. Biol. **28**, 29 (2012).

[3] F. Rizzelli, M. G. Malabarba, S. Sigismund, and M. Mapelli, The crosstalk between microtubules, actin and membranes shapes cell division, Open Biol. **10**, 190314 (2020).

[4] J. G. Carlton, H. Jones, and U. S. Eggert, Membrane and organelle dynamics during cell division, Nat. Rev. Mol. Cell Biol. **21**, 151 (2020).

[5] R. Fraschini, Cytokinesis in eukaryotic cells: The Furrow Complexity at a Glance, Cells **9**, 271 (2020).

[6] A. G. Clark and E. Paluch, Mechanics and regulation of cell shape during the cell cycle, in *Cell Cycle in Development* (Springer, Berlin, 2011), pp. 31–73.

[7] M. P. Stewart, J. Helenius, Y. Toyoda, S. P. Ramanathan, D. J. Muller, and A. A. Hyman, Hydrostatic pressure and the actomyosin cortex drive mitotic cell rounding, Nature (London) **469**, 226 (2011).

[8] E. Fischer-Friedrich, A. A. Hyman, F. Jülicher, D. J. Müller, and J. Helenius, Quantification of surface tension and internal pressure generated by single mitotic cells, Sci. Rep. **4**, 6213 (2015).

[9] S. Nam and O. Chaudhuri, Mitotic cells generate protrusive extracellular forces to divide in three-dimensional microenvironments, Nat. Phys. **14**, 621 (2018).

[10] C. Cadart, L. Venkova, P. Recho, M. C. Lagomarsino, and M. Piel, The physics of cell-size regulation across timescales, Nat. Phys. **15**, 993 (2019).

[11] D. Raucher and M. P. Sheetz, Characteristics of a membrane reservoir buffering membrane tension, Biophys. J. **77**, 1992 (1999).

[12] F. Guilak, G. R. Erickson, and H. P. Ting-Beall, The effects of osmotic stress on the viscoelastic and physical properties of articular chondrocytes, Biophys. J. **82**, 720 (2002).

[13] R. M. Steinman, I. S. Mellman, W. A. Muller, and Z. A. Cohn, Endocytosis and the recycling of plasma membrane, J. Cell Biol. **96**, 1 (1983).

[14] M. Tanaka, K. Fujimoto, and S. Yumura, Regulation of the total cell surface area in dividing dictyostelium cells, Front. Cell Dev. Biol. **8**, 238 (2020).

[15] E. Boucrot and T. Kirchhausen, Endosomal recycling controls plasma membrane area during mitosis, Proc. Natl. Acad. Sci. USA **104**, 7939 (2007).

[16] M. Fürthauer and M. González-Gaitán, Endocytosis and mitosis: A two-way relationship, Cell Cycle **8**, 3311 (2009).

[17] K. S. Gerien and J.-Q. Wu, Molecular mechanisms of contractile-ring constriction and membrane trafficking in cytokinesis, Biophys. Rev. **10**, 1649 (2018).

[18] C. Morris and U. Homann, Cell surface area regulation and membrane tension, J. Membrane Biol. **179**, 79 (2001).

[19] H. T. McMahon and J. L. Gallop, Membrane curvature and mechanisms of dynamic cell membrane remodelling, Nature (London) **438**, 590 (2005).

[20] J. Zimmerberg and M. M. Kozlov, How proteins produce cellular membrane curvature, Nat. Rev. Mol. Cell Biol. **7**, 9 (2006).

[21] D. McCusker and D. R. Kellogg, Plasma membrane growth during the cell cycle: Unsolved mysteries and recent progress, Curr. Opin. Cell Biol. **24**, 845 (2012).

[22] G. Salbreux, G. Charras, and E. Paluch, Actin cortex mechanics and cellular morphogenesis, Trends Cell Biol. **22**, 536 (2012).

[23] T. D. Pollard, Mechanics of cytokinesis in eukaryotes, Curr. Opin. Cell Biol. **22**, 50 (2010).

[24] P. P. D'Avino, M. G. Giansanti, and M. Petronczki, Cytokinesis in animal cells, Cold Spring Harbor Perspect. Biol. **7**, a015834 (2015).

[25] L. Harker-Kirschneck, A. E. Hafner, T. Yao, C. Vanhille-Campos, X. Jiang, A. Pulschen, F. Hurtig, D. Hryniuk, S. Culley, R. Henriques, B. Baum, and A. Šarić, Physical mechanisms of ESCRT-III driven cell division, Proc. Natl. Acad. Sci. USA **119**, e2107763119 (2022).

[26] T. C. Hammarton, Who needs a contractile actomyosin ring? The plethora of alternative ways to divide a protozoan parasite, Front. Cell. Infect. Microbiol. **9**, 397 (2019).

[27] P. Schwille, J. Spatz, K. Landfester, E. Bodenschatz, S. Herminghaus, V. Sourjik, T. J. Erb, P. Bastiaens, R. Lipowsky, A. Hyman, P. Dabrock, J.-C. Baret, T. Vidakovic-Koch, P. Bieling, R. Dimova, H. Mutschler, T. Robinson, T.-Y. D. Tang, S. Wegner, and K. Sundmacher, MaxSynBio: Avenues towards creating cells from the bottom up, Angew. Chem. Int. Ed. **57**, 13382 (2018).

[28] F. Fanalista, A. Birnie, R. Maan, F. Burla, K. Charles, G. Pawlik, S. Deshpande, G. H. Koenderink, M. Dogterom, and C. Dekker, Shape and size control of artificial cells for bottom-u biology, ACS Nano **13**, 5439 (2019).

[29] S. Deshpande, W. K. Spoelstra, M. van Doorn, J. Kerssemakers, and C. Dekker, Mechanical division of cell-sized liposomes, ACS Nano **12**, 2560 (2018).

[30] T. Litschel, B. Ramm, R. Maas, M. Heymann, and P. Schwille, Beating vesicles: Encapsulated protein oscillations cause dynamic membrane deformations, Angew. Chem. Int. Ed. **57**, 16286 (2018).

[31] E. Godino, J. N. López, D. Foschepoth, C. Cleij, A. Doerr, C. F. Castellà, and C. Danelon, De novo synthesized Min proteins drive oscillatory liposome deformation and regulate FtsA-FtsZ cytoskeletal patterns, Nat. Commun. **10**, 4969 (2019).

[32] J. Steinkühler, R. L. Knorr, Z. Zhao, T. Bhatia, S. M. Bartelt, S. Wegner, R. Dimova, and R. Lipowsky, Controlled division of cell-sized vesicles by low densities of membrane-bound proteins, Nat. Commun. **11**, 905 (2020).

[33] Y. Dreher, K. Jahnke, E. Bobkova, J. P. Spatz, and K. Göpfrich, Division and regrowth of phase-separated giant unilamellar vesicles, Angew. Chem. **60**, 10661 (2021).

[34] T. Ruiz-Herrero, T. G. Fai, and L. Mahadevan, Dynamics of Growth and form in Prebiotic Vesicles, Phys. Rev. Lett. **123**, 038102 (2019).

[35] F. Frey and T. Idema, More than just a barrier: Using physical models to couple membrane shape to cell function, Soft Matter **17**, 3533 (2021).

[36] H. Turlier and T. Betz, Unveiling the active nature of living-membrane fluctuations and mechanics, Annu. Rev. Condens. Matter Phys. **10**, 213 (2019).

[37] H. Turlier, B. Audoly, J. Prost, and J.-F. Joanny, Furrow constriction in animal cell cytokinesis, Biophys. J. **106**, 114 (2014).

[38] W. Helfrich, Elastic properties of lipid bilayers: Theory and possible experiments, Z. Naturforsch. C **28**, 693 (1973).

[39] U. Seifert, K. Berndl, and R. Lipowsky, Shape transformations of vesicles: Phase diagram for spontaneous-curvature and bilayer-coupling models, Phys. Rev. A **44**, 1182 (1991).

[40] S. Christ, T. Litschel, P. Schwille, and R. Lipowsky, Active shape oscillations of giant vesicles with cyclic closure and opening of membrane necks, Soft Matter **17**, 319 (2021).

[41] U. Seifert, Configurations of fluid membranes and vesicles, Adv. Phys. **46**, 13 (1997).

[42] E. Evans, Minimum energy analysis of membrane deformation applied to pipet aspiration and surface adhesion of red blood cells, Biophys. J. **30**, 265 (1980).

[43] S. Svetina, M. Brumen, and B. Žekš, Lipid bilayer elasticity and the bilayer couple interpretation of red-cell shape transformations and lysis, Stud. Biophys. **110**, 177 (1985).

[44] B. Bozic, S. Svetina, B. Žekš, and R. E. Waugh, Role of lamellar membrane structure in tether formation from bilayer vesicles, Biophys. J. **61**, 963 (1992).

[45] L. Miao, U. Seifert, M. Wortis, and H.-G. Döbereiner, Budding transitions of fluid-bilayer vesicles: The effect of area-difference elasticity, Phys. Rev. E **49**, 5389 (1994).

[46] H.-G. Döbereiner, E. Evans, M. Kraus, U. Seifert, and M. Wortis, Mapping vesicle shapes into the phase diagram: A comparison of experiment and theory, Phys. Rev. E **55**, 4458 (1997).

[47] M. Deserno, Fluid lipid membranes: From differential geometry to curvature stresses, Chem. Phys. Lipids **185**, 11 (2015).

[48] P. Rowghanian and O. Campàs, Non-equilibrium membrane homeostasis in expanding cellular domains, Biophys. J. **113**, 132 (2017).

[49] L. L. Norman, J. Brugés, K. Sengupta, P. Sens, and H. Aranda-Espinoza, Cell blebbing and membrane area homeostasis in spreading and retracting cells, Biophys. J. **99**, 1726 (2010).

[50] R. B. Lira and R. Dimova, Fusion assays for model membranes: A critical review, in *Multiresponsive Behavior of Biomembranes and Giant Vesicles*, edited by R. Lipowsky, Advances in Biomembranes and Lipid Self-Assembly, Vol. 30 (Elsevier Academic Press, Amsterdam, 2019), Chap. 6, pp. 229–270.

[51] D. Tareste, J. Shen, T. J. Melia, and J. E. Rothman, SNAREpin/Munc18 promotes adhesion and fusion of large vesicles to giant membranes, Proc. Natl. Acad. Sci. USA **105**, 2380 (2008).

[52] F. Nomura, T. Inaba, S. Ishikawa, M. Nagata, S. Takahashi, H. Hotani, and K. Takiguchi, Microscopic observations reveal that fusogenic peptides induce liposome shrinkage prior to membrane fusion, Proc. Natl. Acad. Sci. USA **101**, 3420 (2004).

[53] F. Frey, F. Ziebert, and U. S. Schwarz, Dynamics of particle uptake at cell membranes, Phys. Rev. E **100**, 052403 (2019).

[54] D. Raucher and M. P. Sheetz, Membrane expansion increases endocytosis rate during mitosis, J. Cell Biol. **144**, 497 (1999).

[55] M. Kaksonen and A. Roux, Mechanisms of clathrin-mediated endocytosis, Nat. Rev. Mol. Cell Biol. **19**, 313 (2018).

[56] W. F. Zeno, J. B. Hochfelder, A. S. Thatte, L. Wang, A. K. Gadok, C. C. Hayden, E. M. Lafer, and J. C. Stachowiak, Clathrin senses membrane curvature, Biophys. J. **120**, 818 (2021).

[57] J. Agudo-Canalejo and R. Lipowsky, Critical particle sizes for the engulfment of nanoparticles by membranes and vesicles with bilayer asymmetry, ACS Nano **9**, 3704 (2015).

[58] S. Svetina and B. Žekš, Shape behavior of lipid vesicles as the basis of some cellular processes, Anat. Rec. **268**, 215 (2002).

[59] S. Frémont and A. Echard, Membrane traffic in the late steps of cytokinesis, Curr. Biol. **28**, R458 (2018).

[60] V. G. Almendro-Vedia, F. Monroy, and F. J. Cao, Mechanics of constriction during cell division: A variational approach, PLoS One **8**, e69750 (2013).

[61] E. Beltrán-Heredia, V. G. Almendro-Vedia, F. Monroy, and F. J. Cao, Modeling the mechanics of cell division: Influence of spontaneous membrane curvature, surface tension, and osmotic pressure, Front. Physiol. **8**, 312 (2017).

[62] A. Sain, M. M. Inamdar, and F. Jülicher, Dynamic Force Balances and Cell Shape Changes During Cytokinesis, Phys. Rev. Lett. **114**, 048102 (2015).

[63] D. Zwicker, R. Seyboldt, C. A. Weber, A. A. Hyman, and F. Jülicher, Growth and division of active droplets provides a model for protocells, Nat. Phys. **13**, 408 (2017).

[64] U. Seifert, The concept of effective tension for fluctuating vesicles, Z. Phys. B: Condens. Matter **97**, 299 (1995).

[65] M. Schneider, J. Jenkins, and W. Webb, Thermal fluctuations of large quasi-spherical bimolecular phospholipid vesicles, J. Phys. France **45**, 1457 (1984).

[66] U. Seifert, Fluid membranes in hydrodynamic flow fields: Formalism and an application to fluctuating quasispherical vesicles in shear flow, Eur. Phys. J. B **8**, 405 (1999).

[67] H. Turlier, D. A. Fedosov, B. Audoly, T. Auth, N. S. Gov, C. Sykes, J.-F. Joanny, G. Gompper, and T. Betz, Equilibrium physics breakdown reveals the active nature of red blood cell flickering, Nat. Phys. **12**, 513 (2016).

[68] M. Arroyo and A. DeSimone, Relaxation dynamics of fluid membranes, Phys. Rev. E **79**, 031915 (2009).

[69] S. Deshpande, S. Wunnava, D. Hueting, and C. Dekker, Membrane tension-mediated growth of liposomes, Small **15**, 1902898 (2019).

[70] I. Ivanov, R. B. Lira, T. D. Tang, T. Franzmann, A. Klosin, L. C. da Silva, A. Hyman, K. Landfester, R. Lipowsky, K. Sundmacher, and R. Dimova, Directed growth of biomimetic microcompartments, Adv. Biosys. **3**, 1800314 (2019).

[71] D. Blanken, D. Foschepoth, A. C. Serrão, and C. Danelon, Genetically controlled membrane synthesis in liposomes, Nat. Commun. **11**, 4317 (2020).

[72] P. Virtanen, R. Gommers, T. E. Oliphant, M. Haberland, T. Reddy, D. Cournapeau, E. Burovski, P. Peterson, W. Weckesser, J. Bright, S. J. van der Walt, M. Brett, J. Wilson, K. J. Millman, N. Mayorov, A. R. J. Nelson, E. Jones, R. Kern, E. Larson, C. J. Carey *et al.*, SciPy 1.0: Fundamental algorithms for scientific computing in Python, Nat. Methods **17**, 261 (2020).

[73] S. M. Rafelski and W. F. Marshall, Building the cell: Design principles of cellular architecture, Nat. Rev. Mol. Cell Biol. **9**, 593 (2008).

[74] W. Helfrich, Size distributions of vesicles: The role of the effective rigidity of membranes, J. Phys. France **47**, 321 (1986).

[75] S. A. Safran, Fluctuations of spherical microemulsions, J. Chem. Phys. **78**, 2073 (1983).

[76] S. T. Milner and S. A. Safran, Dynamical fluctuations of droplet microemulsions and vesicles, Phys. Rev. A **36**, 4371 (1987).

[77] A. C. Callan-Jones, V. Ruprecht, S. Wieser, C. P. Heisenberg, and R. Voituriez, Cortical Flow-Driven Shapes of Nonadherent Cells, Phys. Rev. Lett. **116**, 028102 (2016).